Nonlocal spin transport in the light intermetallic alloy Al₂Cu

Justin Ramberger , Ben Kaiser, Paromita Dutta , Mikaela Norum , Turan Birol, and Chris Leighton Department of Chemical Engineering and Materials Science, University of Minnesota, Minneapolis, Minnesota 55455, USA



(Received 5 August 2024; revised 20 October 2024; accepted 30 October 2024; published 18 November 2024)

Transport of spin-polarized electrons injected into light metals is central to the function of numerous spintronic devices and is understood to be limited by Elliott-Yafet spin relaxation. Exploration and quantification of Elliott-Yafet spin relaxation in light metals has not advanced beyond a handful of elements, however, despite the exciting potential for long-range spin transport in alloys. Here, we present a detailed study of spin transport in nonlocal spin valves based on the promising intermetallic alloy Al₂Cu. X-ray diffraction, scanning electron microscopy, energy dispersive x-ray spectroscopy, atomic force microscopy, and electronic transport confirm single-phase, textured, polycrystalline θ -Al₂Cu thin films, particularly after moderate annealing. Measurements on Co-Fe/Al₂Cu-based nonlocal spin valves (including the Hanle effect) then enable full quantification of spin relaxation parameters. The spin diffusion length in Al₂Cu films is found to exceed 100 nm in the low-temperature limit, with Elliott-Yafet constants for phonon and defect scattering that significantly exceed those of Cu. These results are interpreted in light of density functional theory calculations considering spin relaxation hot spots, which also highlight other Al-Cu alloys of high potential interest. This work thus expands the quantitative study of spin transport and relaxation to alloys, laying the foundation for full exploration of light-metal alloys for long-range metallic spin transport.

DOI: 10.1103/PhysRevMaterials.8.114416

I. INTRODUCTION

The injection of spins from ferromagnetic (F) materials into nonmagnetic (N) metals, and their subsequent transport, are central to the function of numerous spintronic devices, including spin valves, spin transfer torque devices, spin pumping devices, etc. [1-4]. For light (i.e., low atomic number Z [5]) metals, the relaxation of injected nonequilibrium spin polarization in N metals is understood to be controlled by the Elliott-Yafet (E-Y) mechanism [6,7]. This is essentially spin relaxation due to electron scattering from phonons or defects in the presence of spin-orbit coupling [1–7]. In the E-Y framework, the spin lifetime τ_s and electron momentum relaxation time τ_e are related by $\tau_s = \beta \tau_e$, where β is an E-Y constant, given in the simplest model by $\beta = (\Delta E / \lambda_{SOC})^2$, where ΔE is the difference in energy of the bands involved in the scattering process and λ_{SOC} is the spin-orbit coupling (SOC) constant [6,7]. In the N metal Cu, for example, $\beta \approx 740$ for phonon scattering [8], meaning that, on average, Cu conduction electrons undergo ~740 momentum-relaxing scattering events prior to spin relaxation. Such β values are known for a number of N metallic elements, including Be, Mg, Al, Cu, Ag, etc., historically from conduction electron spin resonance data [6,7,9,10], and more recently from spintronic studies based on current-perpendicular-plane giant magnetoresistance devices [11] and nonlocal spin valves (NLSVs) [1–4,8,12–26].

Recent studies of the E-Y mechanism in light N metals have emphasized that full quantification of spin relaxation requires a Matthiesen's rule type approach to spin transport

*Contact author: leighton@umn.edu

[8,27,28]. Simply, this expresses the total spin relaxation rate in a given N metal as a sum of the relaxation rates due to each relevant type of scattering center, each with their own E-Y constant [8,27,28]. This gives

$$\frac{1}{\tau_s} = \sum \frac{1}{\tau_{s,i}} = \sum \frac{1}{\beta_i} \frac{1}{\tau_{e,i}},\tag{1}$$

where the index i labels the type of scattering center, such as phonons, grain boundaries, point defects, etc. [8,27,28]. Given the maturity of metallic spintronics, it is perhaps surprising that these β_i are accurately known for few types of scattering, in very few metals [8,27,28]. The β_i for scattering by phonons (~ 740) , grain boundaries (~ 240) and magnetic impurities (~ 1.5) are known for elemental Cu [8,22,29], and defect (~ 4200) and phonon (~ 26000) values have been separated in lighter Al [28], but this is the limit of such quantification, and no such values are known for light-N alloys. These experimental determinations were also made only recently, in NLSVs, exploiting the ability of such devices to cleanly separate charge and spin, thus generating pure, diffusive spin currents [1–4,8,12–29].

A second issue with quantitative understanding of E-Y spin relaxation in N metals is that reconciliation of experimental β values with theoretical calculations has proven challenging. It has been known since the 1960s, for example, that polyvalent elemental N metals such as Be and Mg in Group II, and Al in Group III, have anomalously small β , i.e., unexpectedly fast spin relaxation in comparison to simple E-Y predictions [6,7,9,10]. This was not fully explained until the late 1990s, when Fabian and Das Sarma elaborated the "hot spot" theory of spin relaxation in N metals [30-33]. The essence of their argument is that band crossings at Brillouin zone boundaries, special symmetry points, and accidental degeneracy points (which are common in N metals, particularly polyvalent, high-Fermi-energy ones) lead to localized areas on the Fermi surface where $\Delta E \rightarrow 0$, thus creating hot spots of highly efficient spin relaxation, which can dominate the average β [30–33]. The small size of these hot spots in momentum space makes accurate calculations of β challenging, but this approach nevertheless led to the first calculation of an E-Y constant in Al in quantitative agreement with experiment [30,31], which remains the only such achievement to our knowledge. This required an involved calculation employing \sim 10 000 momentum-space grid points.

The successes and insights provided by the hot spot theory of E-Y spin relaxation also generate intriguing predictions [30–33], which have not yet been experimentally validated. It is apparent, for example, that avoidance of spin relaxation hot spots in the vicinity of the Fermi surface of N metals could realize much larger β values, i.e., far slower spin relaxation than in currently employed N metals. There are two clear strategies to pursue this. The first is to tune the position of the Fermi energy $(E_{\rm F})$ in a base light N metal such as Al or Mg to avoid the energies of the most problematic hot spots. First-principles calculations employing rigid band approximations in fact suggest that reduction of $E_{\rm F}$ in polyvalent Al and Mg could realize remarkable 10^2 – 10^3 -fold enhancements of β [30–33]. Substitutional solid solution alloys such as $Al_{1-x}M_x$ where M is a lower-valence-electron element such as Cu or Mg present one potential route to such tuning, although solubility limits (which would limit the extent of modulation of $E_{\rm F}$), and alloy scattering (which would decrease τ_e , counteracting the effects of enhanced β in $\tau_s = \beta \tau_e$) are potential challenges. Significantly, however, little if any work has been performed in this direction.

The second possible strategy to enhance β is to add alloying elements to light N metals such as Al that induce a transformation to a crystal structure with minimal hot spots near the Fermi surface. Atomically ordered alloys (intermetallics) based on all-light-metal, low-SOC, N elements thus become of high interest, provided they have band structures with manageable hot spots near E_F , and low resistivity. Such alloys could realize long τ_e , large β , and thus long τ_s , thereby generating long spin diffusion lengths, $\lambda_{\rm N} = (D\tau_{\rm s})^{1/2}$. Again, however, it should be emphasized that little if any exploration has been performed in this direction. This is despite the potential for fundamental advances in the understanding of spin relaxation, as well as the possible technological benefits. Spin accumulation sensors based on metallic NLSVs, for example, are leading candidates for nextgeneration low-resistance-area-product read heads in hard disk drives [34–38], which would benefit exponentially from longer λ_N [39]. Spin interconnect concepts are also highly attractive for low-power-dissipation microelectronics [27,40] and could be realized with standard polycrystalline metal films if N alloys with sufficiently large β (and therefore λ_N) were developed.

Based on the above, exploration of the spin transport properties of light intermetallic N alloys is well overdue. One compelling starting point for such exploration is the Al-Cu system. This is because of the simple binary nature of this alloy system, the low-Z (low-SOC) character of Al

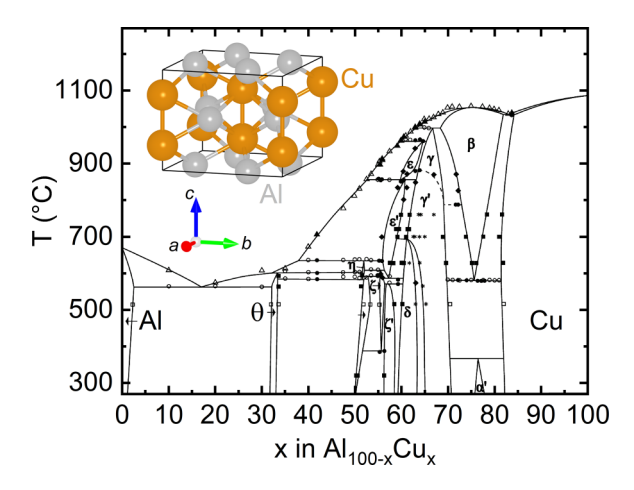


FIG. 1. Al-Cu binary alloy phase diagram adapted from the data of Zobac *et al.* [41] and Ponweiser *et al.* [42]. The θ phase of Al₂Cu is labeled, along with the other known ordered phases. Inset: Crystal structure of θ -Al₂Cu with Al and Cu shown in gray and orange, respectively (generated by VESTA [65]). The solid line is the unit cell outline and the crystal axes are shown.

and Cu, the well understood β_i in elemental Al [28] and Cu [8,22,29], and the existence of several ordered intermetallics in this system. The latter include Al_2Cu (space group I4/mcm), AlCu(C2/m), $Al_2Cu_3(R-3m)$, and $Al_4Cu_9(P-43m)$, as well as several high-temperature/metastable phases, as shown in the phase diagram in Fig. 1 [41,42]. While all of these phases are unexplored from the spin transport perspective, θ -phase Al₂Cu [see Fig. 1(a)] is of particular interest. This ordered alloy has been heavily studied in metallurgy (due to its central role in precipitation strengthening of Al alloys [43]), is Al-rich (i.e., rich in the lowest-Z, highest- β elemental component), has high structural symmetry (I4/mcm, see the inset to Fig. 1 for a schematic of the layered θ -Al₂Cu crystal structure), and has been reported to have relatively low resistivity (ρ). ρ values at 300 K are as low as \sim 10 $\mu\Omega$ cm in films [44–46] and 7.5 $\mu\Omega$ cm in bulk [44,48], the corresponding residual resistivities (ρ_0) being 2.5 [44,46] and 0.9 $\mu\Omega$ cm [44,48], respectively. Al₂Cu has in fact been explored for potential applications in conventional microelectronic interconnects, due to favorable resistivity scaling compared to Cu, resistance to electromigration, good gap filling characteristics during reflow, and the possibility of use without wetting liners or diffusion barriers [44–53].

In light of the above, here we combine thin film deposition with x-ray diffraction (XRD), scanning electron microscopy (SEM), energy dispersive x-ray spectroscopy (EDS), atomic force microscopy (AFM), and electronic transport measurements to demonstrate fabrication of single-phase, textured, polycrystalline θ -Al₂Cu, particularly after vacuum annealing. In a narrow window centered around 33 at.% Cu, residual resistivity (ρ_0) as low as 3–4 $\mu\Omega$ cm is obtained in (112)-textured films. Such films are then integrated into Co₇₈Fe₂₂/ θ -Al₂Cu NLSVs, in which full characterization of N spin transport is achieved. Room-temperature $\lambda_N \approx 60$ nm is obtained, increasing to \sim 115 nm at low temperature (T), below \sim 20 K. E-Y analyses based on both separation-dependent NLSV measurements and the electrical Hanle effect then enable

determination of phonon and defect scattering β values, which are found to substantially exceed those of Cu, but not Al. These results are interpreted in light of density functional theory (DFT) calculations considering spin relaxation hot spots, which also highlight potential interest in the related η' -AlCu system as a next target. This work thus expands the study of spin transport in the nonlocal geometry to alloys, opening the door to full exploration of light N solid solution and intermetallic alloys for spin relaxation hot spot mitigation and long-range spin transport.

II. METHODS

Film depositions employed ultrahigh vacuum (UHV) evaporation in a system with a base pressure of $\sim 1 \times 10^{-11}$ Torr and deposition pressures of $\sim 1 \times 10^{-9}$ Torr. Al-Cu alloys were co-deposited from electron-beam evaporators loaded with 99.999% pure Al and Cu, onto room-temperature Si/Si-N(300 nm) substrates that were continuously rotated. The total $Al_{1-x}Cu_x$ deposition rate was held at 5 Å/s, individual fluxes being controlled by two independent quartz-crystal rate monitors. Films of thickness 30–300 nm were prepared. Some films were vacuum annealed for comparison to as-deposited films, for 2 h at 300 or 400 °C (as specified), in a vacuum annealer with a base pressure of $\sim 1 \times 10^{-7}$ Torr. Films were then characterized by SEM and EDS in a Thermo Fisher Scientific Apreo 2S SEM with an Oxford Instruments Ultimax 100 mm² EDS system. XRD and AFM were also performed, using a Bruker D8 Discover and a Bruker Nanoscope V Multimode 8 AFM in PeakForce Tapping mode [54]. Film resistivity measurements (4.2 to 300 K) employed the van der Pauw method, utilizing a Lakeshore 372 AC resistance bridge and a Lakeshore 3708 preamplifying channel scanner sourcing 100 µA at 13.7 Hz.

NLSVs were fabricated by evaporation through shadow masks formed from bilayer resists patterned by electron beam lithography. First deposited were 16-nm-thick Co₇₈Fe₂₂ F layers, followed by 300-nm-thick Al₂Cu N channels, using the multiangle deposition and liftoff employed in prior work [8,22,28,29,55,56] and detailed in Supplemental Material Sec. A [57]. This enables single-shot deposition of NLSVs without breaking vacuum, resulting in low-resistance, i.e., "transparent," interfaces [8,22,28,29,55,56]. After liftoff, NLSVs were vacuum annealed at 300 °C for 2 h; higher temperatures were found to unacceptably degrade performance, likely due to F/N intermixing. Device dimensions were measured by both SEM and AFM, the N channel widths being ~250 nm and the F injector and detector widths being ~ 150 and ~ 100 nm, respectively. Charge and spin transport measurements on NLSVs were made from 5 to 300 K in a helium flow cryostat with a 9 T superconducting magnet utilizing a Lakeshore 372 AC resistance bridge and a Lakeshore 3708 preamplifying channel scanner sourcing 100 µA at 13.7 Hz.

Electronic structure calculations on ordered Al-Cu alloys were performed using DFT, both with and without SOC. These calculations utilized the full-potential linearized augmented plane-wave (FP-LAPW) method implemented in the WIEN2K package [58]. The generalized gradient approximation (GGA) within the Perdew-Burke-Ernzerhof (PBE) formalism was employed as the exchange-correlation

functional [59]. Muffin-tin sphere radii of 2.10 (2.25) Bohr for Al and 2.38 (2.29) Bohr for Cu were used for AlCu (Al₂Cu), and the size of the basis set was chosen by setting the $R_{min}k_{max}$ parameter to 7.0. An $8 \times 8 \times 8$ mesh was used for both compounds to calculate the self-consistent charge densities, while denser k meshes were used to generate Fermi surfaces, specifically $27 \times 18 \times 27$ for AlCu and $24 \times 24 \times 24$ for Al₂Cu. In order to avoid DFT errors in structure prediction, the experimental values of lattice parameters and atomic positions were used for most of the calculations [60]. As discussed below, however, to check the impact of this assumption, additional calculations were also made with relaxed structures. η' -AlCu adopts the base-centered monoclinic space group C2/m (space group number 12), and θ -Al₂Cu adopts the body-centered tetragonal space group I4/mcm (space group number 140). For both compounds, primitive unit cells (6 atoms for Al₂Cu and 10 atoms for AlCu) were used.

III. RESULTS AND ANALYSIS

As discussed in the Introduction, the Al-Cu binary alloy phase diagram and the crystal structure of θ -Al₂Cu are show in Fig. 1. It is worth noting from Fig. 1 that θ -Al₂Cu is not a line compound, instead forming over a finite composition window of \sim 2 at.%. The structure is tetragonal (*I4lmcm*) and layered, featuring alternating planes of Al and Cu along the c axis [61]. To explore the formation of this and other Al-Cu phases, deposition of Al_{1-x}Cu_x thin films was performed over a wide x range, focusing in particular near x = 0.33, i.e., in the vicinity of Al₂Cu.

A. Transport, structural, and chemical characterization

A wide-x-range survey was first performed by carrying out $\rho(T)$ measurements at 20 compositions, in ~30-nm-thick $Al_{1-x}Cu_x$ films. As shown in Figs. 2(a) and 2(b), this reveals a dome-shaped maximum in both the 295 K and low-T (residual) resistivities, centered on \sim 50 at.%, as would be expected from simple alloy scattering [62]. Superimposed on this dome, however, is a sharp dip in Figs. 2(a) and 2(b) around 33 at.% Cu (note the log₁₀ scales), strongly suggestive of the formation of an ordered alloy (intermetallic Al₂Cu). This is evidenced even in the as-deposited state [black points in Figs. 2(a) and 2(b)], although the resistivities substantially decrease after vacuum annealing for 2 h at 400°C [orange points in Figs. 2(a) and 2(b)], as expected. At 33 at.% Cu, the 300 K and residual resistivities after annealing are in fact in reasonable agreement with prior work on θ -Al₂Cu films of comparable thickness [44–53]. Some evidence of the formation of the η' phase near 50 at.% (see Fig. 1) is also apparent in Figs. 2(a) and 2(b), along with a more surprising resistivity minimum near 40 at.% Cu. As shown in Supplemental Material Fig. S1 [57], this unexpected resistivity minimum around 40 at.% Cu is associated with substantial coarsening of a microstructure formed from coexisting Al₂Cu and AlCu, an incidental finding in the current context. Figure 2(c) then shows the residual resistivity ratio (RRR) deduced from Figs. 2(a) and 2(b). The RRR versus x is asymmetric due to the differing transport characteristics of polycrystalline thin-film Al [22,28,56] and Cu [8,22,55] at this thickness, and again has

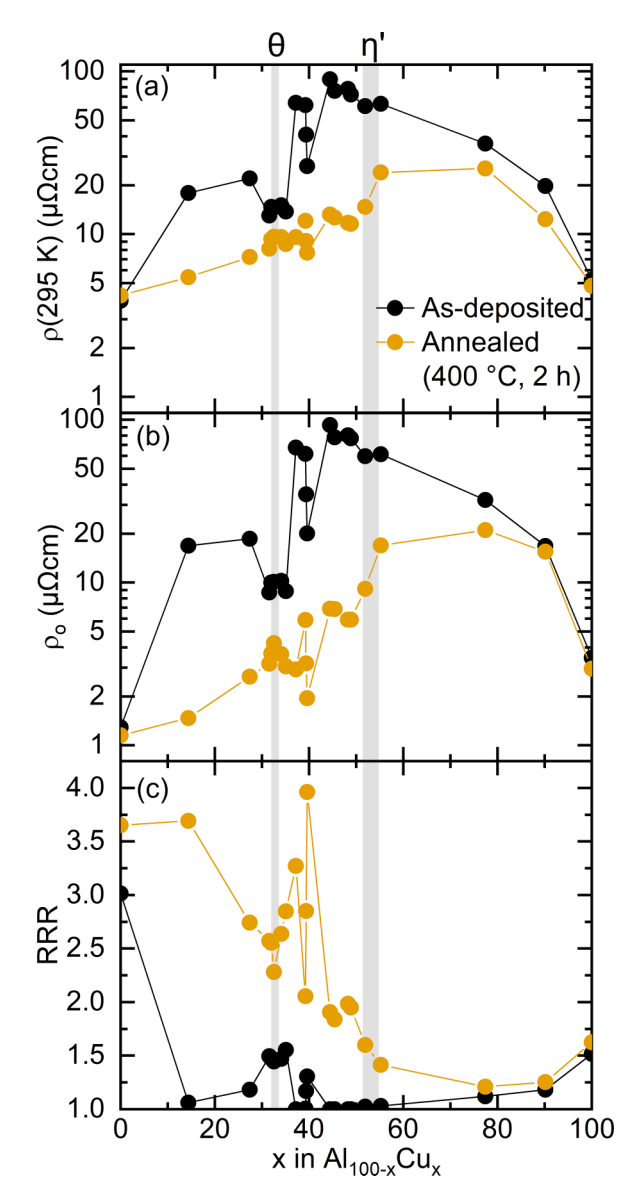


FIG. 2. Cu content dependence of (a) the 295 K resistivity $[\rho(295 \text{ K})]$, (b) the residual resistivity (ρ_0) , and (c) the residual resistivity ratio (RRR) of 30-nm-thick $Al_{1-x}Cu_x$ films. Data are shown for both as-deposited films (black) and after vacuum annealing at 400°C for 2 h (gold). The approximate windows of formation of the θ and η' phases are marked in gray; these are based on the widest ranges in the equilibrium Al-Cu phase diagram [41,42]. Cu concentrations are from energy dispersive x-ray spectroscopy (EDS). Note the \log_{10} scale in panels (a), (b).

a maximum near 40 at.% Cu, but, most importantly, displays clear features centered on 33 at.% Cu. Explicitly, the formation of ordered Al_2Cu is evidenced directly in the as-deposited data (in which the RRR peaks), becoming less distinct after annealing, likely related to the unusual behavior at \sim 40 at.% Cu.

On the basis of Fig. 2, detailed structural and chemical characterizations were performed on 300-nm-thick $Al_{1-x}Cu_x$ films with $x \approx 0.33$. Figure 3(a) shows example EDS data from a film determined (by EDS) to have 33 at.% Cu, revealing only Al, Cu, a Si substrate signal, and typical SEM

contaminants. The inset to Fig. 3(a) shows a representative AFM image from such a 300-nm-thick film, revealing a nanograined (~45 nm grain size) polycrystalline morphology, and 3-nm root-mean-square roughness. The XRD data in Fig. 3(b) (see Supplemental Material Fig. S2 [57] for raw twodimensional detector images) confirm the formation of the θ phase of Al₂Cu, both before and after vacuum annealing. As deposited, the (110), (112), (202), (222), and (213) peaks of θ -Al₂Cu are observed, confirming the θ phase (the blue lines at the bottom correspond to a θ -Al₂Cu reference pattern [61]), the relative peak intensities indicating (112) texture. [The asterisked peaks in Fig. 3(b) are from the Si/Si-N substrate (see also Fig. S2 [57])]. Upon annealing, the XRD peaks sharpen, and the relative intensity of the (112) peak further increases, indicating yet stronger (112) texture. As shown in Supplemental Material Fig. S3 [57], the grain size changes little with annealing, however, meaning that the annealing-driven peak width decrease in Fig. 3(b) derives from a decrease in microstrain. The (vertical) grain size from Scherrer analysis of peak widths is then >100 nm, substantially larger than the in-plane grain size from AFM, indicating columnar grains, as is common in polycrystalline metal films. The extracted lattice parameters are $a = 6.04 \pm 0.01$ Å and $c = 4.86 \pm 0.01$ Å after annealing, in reasonable agreement with the accepted bulk values (a = 6.067 and c = 4.877 Å [61]), confirming essentially full strain relaxation of these 300-nm-thick films. A uniform microstructure, practically free of second-phase regions, is evidenced by Fig. 3(c), which shows an SEM image with corresponding Cu and Al EDS maps. Aside from a low volume fraction of Cu-deficient regions, the micron-scale structure and composition appear uniform (see Supplemental Material Figs. S1 and S4 for further details [57]).

B. Spin transport in nonlocal spin valves

As per Sec. II (Methods), integration of θ -Al₂Cu films into transparent-interface $Co_{78}Fe_{22}(16 \text{ nm})/\theta$ -Al₂Cu (300 nm)-based NLSVs was achieved by room-temperature multiangle UHV electron beam evaporation [56] into resist masks defined by electron beam lithography, followed by liftoff [8,22,28,29,55,56]. The resulting structures were then vacuum annealed at 300°C for 2 h, to minimize resistivity. An SEM image of a typical device is presented in Fig. 4(a), showing the θ -Al₂Cu channel, Co₇₈Fe₂₂ injector and detector contacts, and the arrangement of injected charge current and detected voltage for a nonlocal measurement. As noted in the figure caption, the Co₇₈Fe₂₂ layers present weak contrast in Fig. 4(a) due to their low thickness (16 nm) relative to the channel (300 nm), while the shadowing of the "vertical" features in Fig. 4(a) arises due to small angular misalignment of the Cu and Al evaporation sources (see Sec. II and Supplemental Material Section A [57] for details). Complementary AFM images are presented in Figs. 4(b) and 4(c), where the rippling of the 300-nm-thick θ -Al₂Cu channel over the 16-nm-thick injector and detector contacts is clear upon close inspection.

Turning to electrical characterization of such NLSVs, Fig. 4(d) first shows $\rho(T)$ from local measurements of the 300-nm-thick θ -Al₂Cu channel. This reveals typical metallic form, this particular NLSV having $\rho_0=7.4\,\mu\Omega cm$; this is elevated

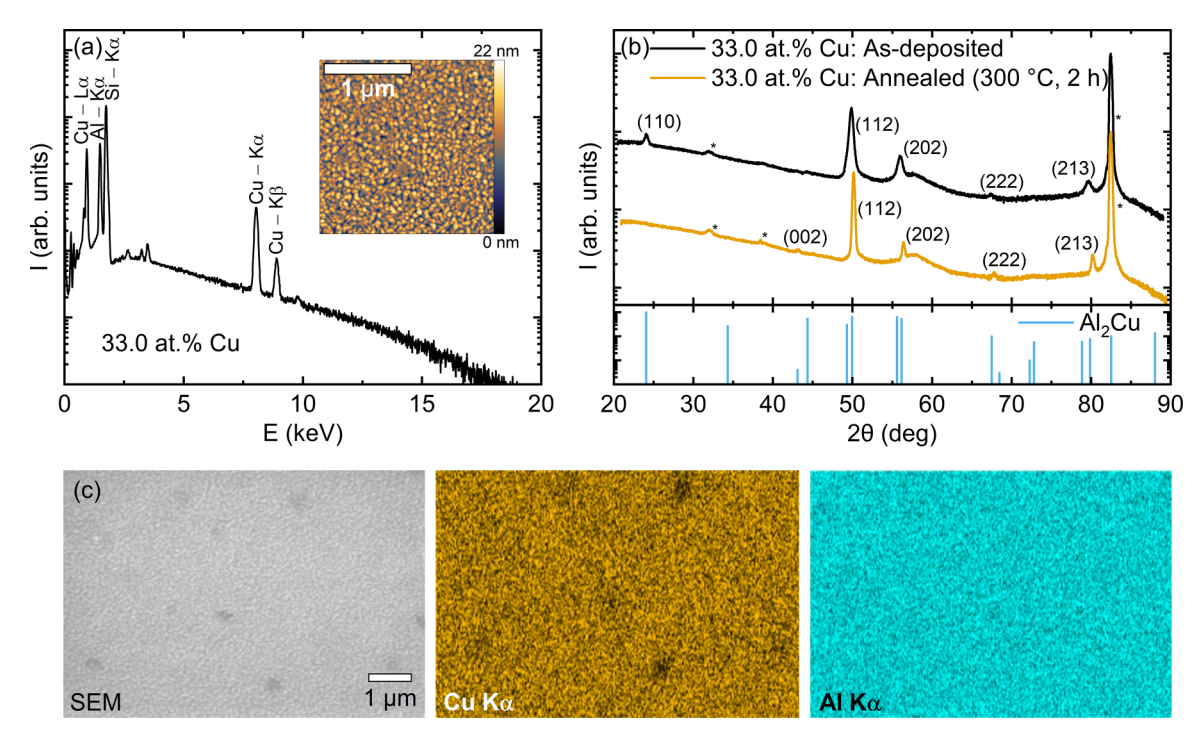


FIG. 3. (a) Energy dispersive x-ray spectroscopy (EDS) data from an as-deposited 300-nm-thick $Al_{66}Cu_{33}$ film. The small peaks in the 2.5–3.0 keV range are from common SEM contaminants and the Si/Si-N substrate. Inset: Atomic force microscopy (PeakForce tapping mode [54]) image of the same film. (b) Corresponding x-ray diffraction patterns from as-deposited (black) and vacuum-annealed films (gold, 300°C, 2 h). The peaks are indexed, the asterisks mark reflections from the substrate, and a reference powder pattern for θ -Al₂Cu [61] is shown in blue at the bottom. (c) Scanning electron microscopy image of the same film (annealed at 300°C for 2 h), along with corresponding Cu and Al EDS maps. A 1-µm scale bar is shown.

relative to the continuous films in Fig. 2(b), but within reasonable bounds given the 250-nm linewidth and lower annealing temperature (see Sec. II). Figure 4(e) then shows nonlocal resistance (R_{NL}) vs applied in-plane magnetic field (H_{\parallel}) data at multiple T, for a fixed F injector-detector separation (d) of 240 nm. Abrupt switching between well-defined parallel (P) and antiparallel (AP) states is seen at all T, enabling unambiguous determination of $\Delta R_{\rm NL}$, the NLSV spin signal. This $\Delta R_{\rm NL}$ is plotted versus T in Fig. 4(f), at six example separations. $\Delta R_{\rm NL}$ rolls off monotonically with increasing T, with the expected progressive decrease in magnitude with increasing d [note the log scale $\Delta R_{\rm NL}$ axis in Fig. 4(f)]. At the shortest separations probed (240 nm), the spin signal in the low-T limit exceeds 0.1 m Ω , comparable to similar-sized transparent-interface NLSVs based on other N-metal channel materials [8,22,28,29,55,56]. Notably, $\Delta R_{\rm NL}(T)$ is monotonic, with no evidence of the characteristic low-T downturn associated with the spin-transport Kondo effect [8,22,23,29,55]. Based on our prior work on transparent-interface metallic NLSVs, this is absent only for channel materials that do not support local moment formation on magnetic impurities diffused in from the F electrodes, typically related to high $E_{\rm F}$ in the N metal [8,22,29,55]. $E_{\rm F}$ is indeed high in θ -Al₂Cu (10.7 eV from the DFT calculations discussed below), consistent with this notion. (Note that we define all E_F values in this work relative to the bottom of the highest filled band). This absence of Kondo effects in Al₂Cu-based NLSVs is an attractive attribute in terms of applications, as these effects can diminish spin signals even at room temperature in NLSVs with unfavorable F/N combinations [55].

Quantitative analysis was performed by fitting $\Delta R_{\rm NL}$ versus d data at each T [five example temperatures are shown in Fig. 5(a)] to the standard Takahashi-Maekawa model [39] in the transparent-interface limit. This is a one-dimensional model for spin transport in NLSVs, based on the Valet-Fert approach [63], giving

 $\Delta R_{NL}(d,T)$

$$=4\frac{\alpha^{2}R_{F}^{2}}{(1-\alpha^{2})^{2}R_{N}}\frac{\exp(-d/\lambda_{N})}{\left[1+\frac{2R_{F}}{(1-\alpha^{2})R_{N}}\right]^{2}-\exp(-2d/\lambda_{N})}.$$
 (2)

Here, α is the injected current spin polarization at the F interface, and $R_N = \rho_N \lambda_N / w_N t_N$ and $R_F = \rho_F \lambda_F / w_N w_F$ are the spin resistances of the N and F, respectively; ρ_N , w_N , and t_N are the resistivity, width, and thickness of the N channel, respectively, and ρ_F , λ_F , and w_F are the resistivity, spin diffusion length, and width of the F electrodes, respectively [39]. As in our prior work on NLSVs based on other materials [8,22,28,29,55,56], we carefully measured all device dimensions by SEM, measured $\rho_N(T)$ in the same devices [Fig. 4(d)], and determined $\rho_F(T)$ from measurements of separate F nanowire devices with near-identical dimensions. A careful analysis, fully documented in our prior work, was then used to fix $\lambda_F(T)$ from the measured $\rho_F(T)$ [56]. This procedure leaves only α and λ_N as free parameters, the slope of the fits to $\Delta R_{NL}(d)$ in Fig. 5(a) being determined solely

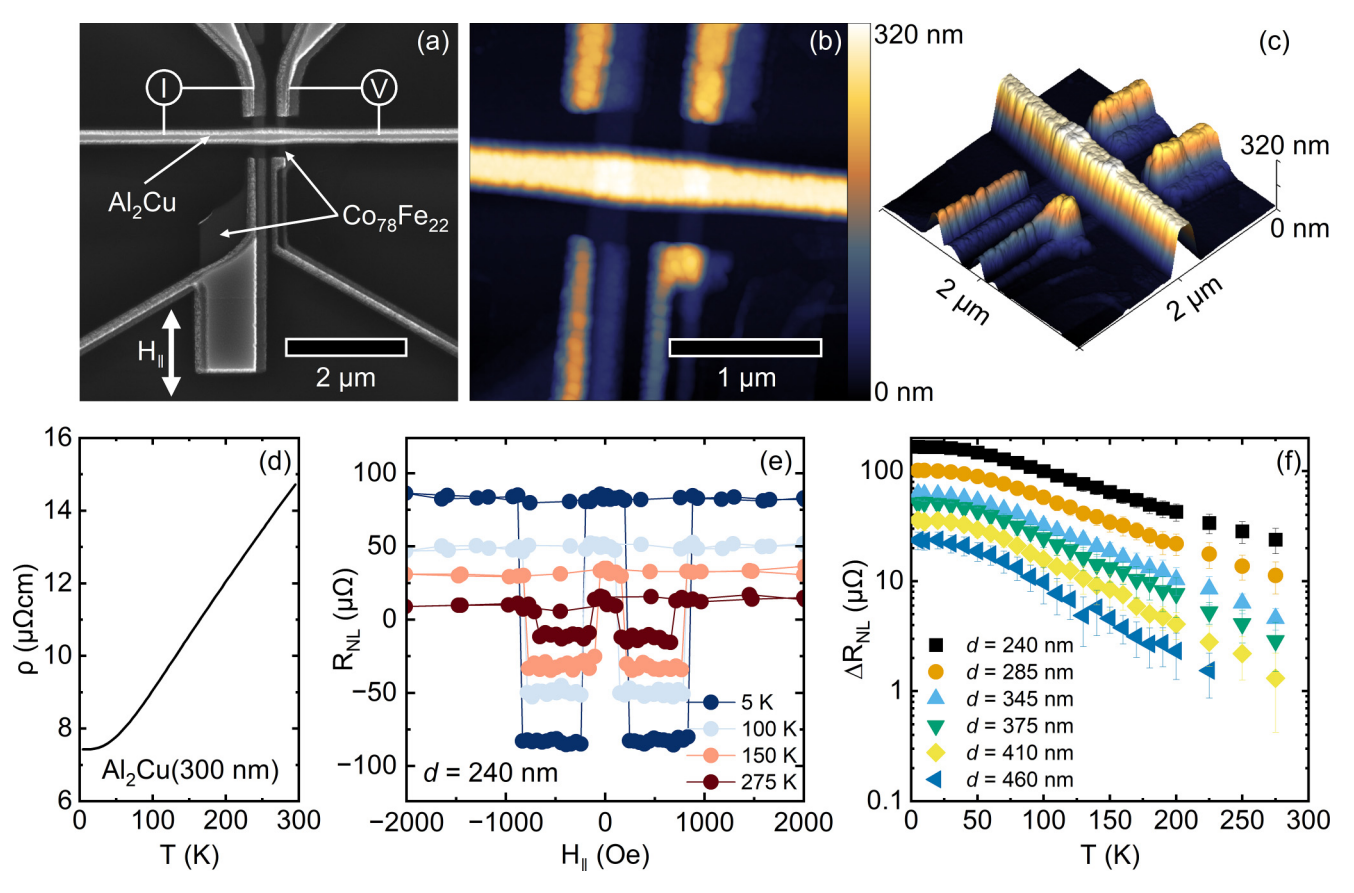


FIG. 4. (a) Scanning electron microscopy image of a $\text{Co}_{78}\text{Fe}_{22}/\theta\text{-Al}_2\text{Cu}$ nonlocal spin valve (NLSV), showing the charge current (*I*), nonlocal voltage (*V*), and in-plane applied magnetic field (H_{\parallel}). A 2-μm scale bar is shown. The shadowing of vertical features is due to the codeposition of Al and Cu, as described in the text. The contrast due to $\text{Co}_{78}\text{Fe}_{22}$ is relatively weak due to the low film thickness (16 nm). (b), (c) Planar and projection atomic force microscopy images of a similar NLSV. The rippling of the thick θ -Al₂Cu channel over the thin $\text{Co}_{78}\text{Fe}_{22}$ contacts is visible upon close inspection. (d) Temperature (*T*) dependence of the resistivity (ρ) of the θ -Al₂Cu(300 nm) channel in a vacuum-annealed $\text{Co}_{78}\text{Fe}_{22}(16\,\text{nm})/\theta$ -Al₂Cu(300 nm) NLSV. (e) Offset-subtracted H_{\parallel} dependence of the nonlocal resistance (R_{NL}) of the same NLSV at separation $d=240\,\text{nm}$ and several temperatures. (f) *T* dependence of the NLSV spin signal ΔR_{NL} at various *d*. Error bars in panel (f) are one standard deviation on ΔR_{NL} .

by λ_N , meaning that the two parameters are easily separable. The resulting fits in Fig. 5(a) are good (note that this is a log-linear plot), revealing an essentially ideal exponential fall off at high d, as well as the onset of the low-d upturn expected in transparent-interface devices (due to spin back-diffusion effects [39]).

The extracted $\lambda_N(T)$ and $\alpha(T)$ are shown in Figs. 5(b) and 5(c). In these 300-nm-thick θ -Al₂Cu channels, λ_N is found to be \sim 60 nm at room temperature, increasing monotonically to \sim 115 nm in the low-T limit (below \sim 20 K). These values can be compared to as-deposited thick-film-limit λ_N values of approximately 200 and 600 nm at room and low temperature in Cu [8,22,55], and approximately 400 and 1500 nm at room and low temperature in Al [22,28,56]. As discussed in more detail below, however, the shorter λ_N in θ -Al₂Cu is due, in significant part, to the higher ρ and lower τ_e , i.e., less efficient charge transport. Moving to Fig. 5(c), the extracted $\alpha(T)$ is seen to be quite T-independent, as we previously reported in Co₇₅Fe₂₅/Al NLSVs, reflecting the high Curie temperature and substantial magnetocrystalline anisotropy of such alloys [56]. The polarization of \sim 35% is suppressed relative to our recent report on Co₇₅Fe₂₅/Al NLSVs [56], due to the slight shift in composition here (to $Co_{78}Fe_{22}$) and the thermal annealing employed to minimize the θ -Al₂Cu resistivity. This annealing likely interdiffuses the $Co_{78}Fe_{22}/\theta$ -Al₂Cu interface to some degree, degrading the interfacial spin polarization, and limiting the maximum annealing temperature (see Sec. II). This not a major concern here due to the primary focus on probing spin relaxation in the Al₂Cu bulk rather than interfacial spin injection. We note, however, that the presence of interdiffusion makes the absence of any Kondo effects in $\Delta R_{\rm NL}(T)$ [Fig. 4(f)], $\lambda_{\rm N}(T)$ [Fig. 5(b)], and $\alpha(T)$ [Fig. 5(c)] all the more remarkable, as such spin transport Kondo effects are enhanced by F/N intermixing [8,22,23,29,55].

As noted in the Introduction, deeper analysis of spin relaxation requires extraction of E-Y β values, from comparisons of τ_e and τ_s . To this end, Fig. 6(a) shows $\tau_e(T)$ extracted from the $\rho_{\rm N}(T)$ in Fig. 4(d), using $\tau_e(T) = 3/(\rho(T)N(E_{\rm F})v_{\rm F}^2\,e^2)$ where $N(E_{\rm F})$ is the density of states at the Fermi energy, $v_{\rm F}$ is the Fermi velocity, and e is the electronic charge [62]. Using the DFT-calculated $E_{\rm F}=10.7$ eV and $v_{\rm F}$ determined from $E_{\rm F}$ via a free-electron model [62], along with $N(E_{\rm F})$ from DFT, the resulting $\tau_e(T)$ in Fig. 6(a) increases from 1.5 fs at 295 K to 2.9 fs at low T. Figure 6(b) compares these

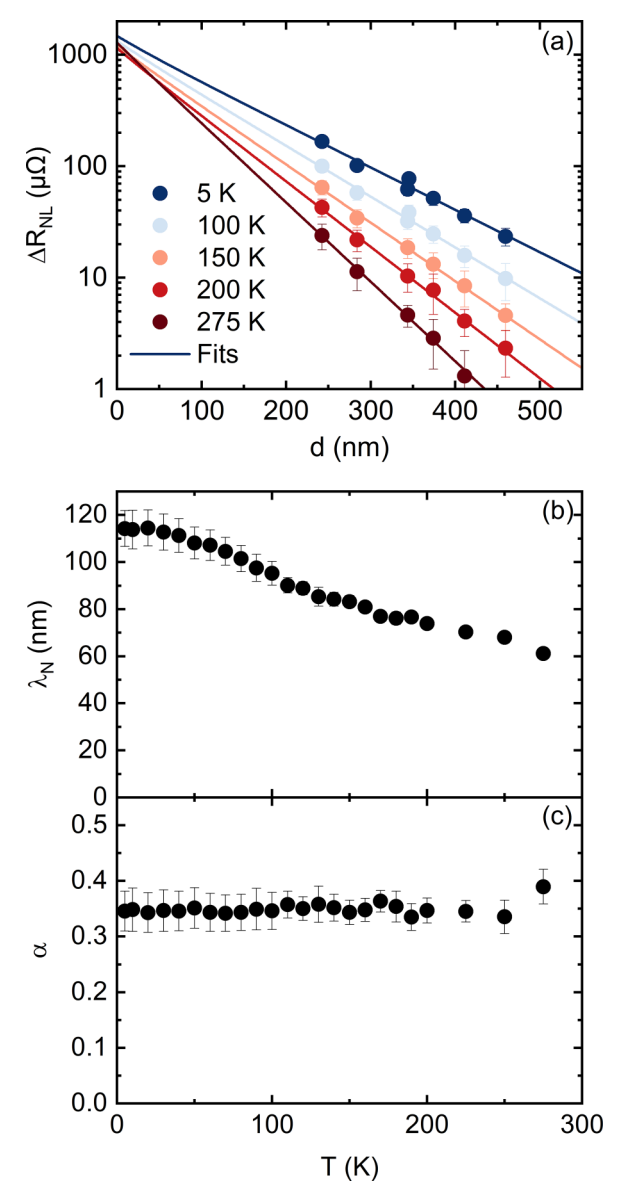


FIG. 5. (a) Spin signal ($\Delta R_{\rm NL}$, solid points) vs separation (d) at various temperatures for vacuum-annealed ${\rm Co_{78}Fe_{22}(16\,nm)}/\theta{\rm -Al_2Cu(300\,nm)}$ nonlocal spin valves. The solid lines are fits to the Takahashi-Maekawa model described in the text [39]. Temperature (T) dependence of (b) the extracted spin diffusion length ($\lambda_{\rm N}$) and (c) the extracted current spin polarization (α). Error bars in panel (a) are one standard deviation; error bars in panels (b), (c) are the standard errors from the fits in panel (a).

values to the spin transport equivalent, $\tau_s(T)$, determined from $\tau_s(T) = \lambda_N(T)^2/D(T)$, where $\lambda_N(T)$ comes from Fig. 5(b) and $D(T) = (\rho(T)N(E_F)e^2)^{-1}$, i.e., through the use of an Einstein relation [62]. This results in the black points in Fig. 6(b), which show $\tau_s(T)$ decreasing from 3.6 ps at low T to 2.0 ps at 275 K. These values from d-dependent measurements of NLSVs (Fig. 5) were also independently checked via Hanle effect measurements. An example (5 K) Hanle data set is shown in the inset to Fig. 6(b), which plots $\Delta R_{\rm NL}$ as a function of out-of-plane applied magnetic field H_{\perp} . The solid line here is a fit to a model for Hanle spin precession accounting for the effects of magnetization rotation in the F electrodes [64]. This

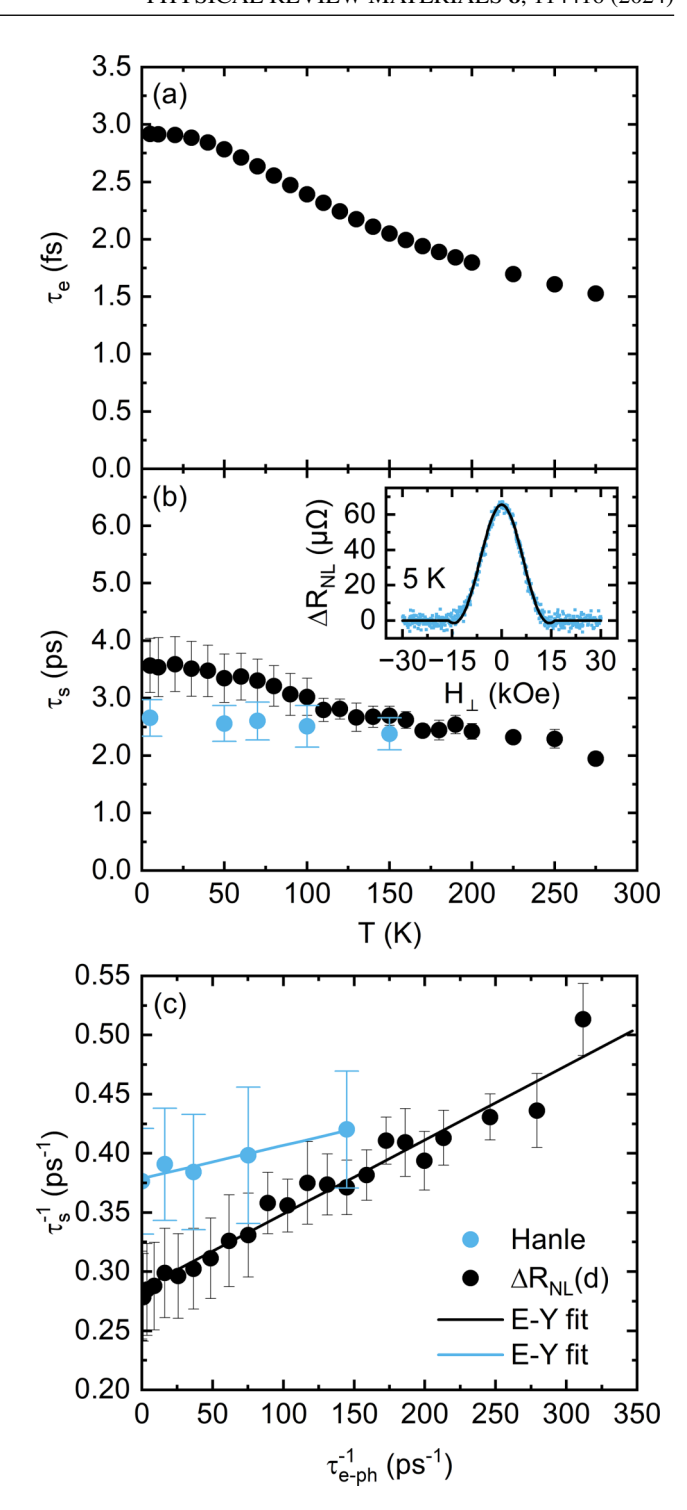


FIG. 6. Temperature (T) dependence of (a) the momentum relaxation time (τ_e), and (b) the spin lifetime (τ_s) from measurements on vacuum-annealed $\text{Co}_{78}\text{Fe}_{22}(16\,\text{nm})/\theta\text{-Al}_2\text{Cu}(300\,\text{nm})$ nonlocal spin valves. The black points in panel (b) are from separation (d)-dependent data, while the blue points are from Hanle effect measurements of the type illustrated in the inset (nonlocal spin signal vs out-of-plane field, in this example at $T=5\,\text{K}$ and $d=345\,\text{nm}$). (c) "Elliott-Yafet plot," i.e., τ_s^{-1} vs $\tau_{e\text{-ph}}^{-1}$, where $\tau_{e\text{-ph}}^{-1}$ is the phonon scattering part of τ_e^{-1} . The implicit variable here is T, and data are shown from both the d dependence and the Hanle effect. The solid lines are straight-line fits yielding the defect and phonon Elliott-Yafet constants from the intercept and slope, respectively. All error bars are propagated standard errors.

gives

$$\Delta R_{NL}(H_{\perp}) = S_0 \left(1 - \left(\frac{H_{\perp}}{H_k} \right)^2 \right) \int_{-w_F^{\text{inj}}}^0 \int_d^{d+w_F^{\text{det}}} \int_0^{\infty} \frac{1}{\sqrt{4\pi Dt}} e^{\frac{x_{\text{inj}} - x_{\text{det}}}{4Dt}} \cos(\omega_L t) e^{-\frac{t}{\tau_S}} dt \, dx_{\text{det}} dx_{\text{inj}},$$
(3)

where S_0 is a normalization factor for the zero-field signal, H_k is the anisotropy field of the F (Co₇₈Fe₂₂ here), ω_L is the Larmor frequency, which is dependent on H_{\perp} and the gyromagnetic ratio, and t and x are the spin propagation time and distance [64]. The "inj" and "det" subscripts here denote the injector and detector. It is important to note that this model does not take into account the complication of back diffusion of injected spins into the Finjector [39,64]. This is not an issue as the Hanle data presented here were acquired at d = 345nm, i.e., three times or more λ_N , which makes relaxation in the bulk of the N channel dominant over N/F interface effects [64]. The thus-extracted Hanle $\tau_s(T)$ data are shown as blue points in Fig. 6(b). The $\Delta R_{\rm NL}(d)$ (black) and Hanle (blue) measurements agree to within 25% at the lowest T, improving to within 12% by 150 K, above which Hanle measurements became impractical due to signal-to-noise issues in the employed data collection approach.

Figure 6(c) then shows an "Elliott-Yafet plot" of τ_s^{-1} versus $\tau_{\scriptscriptstyle o}^{-1}$, i.e., spin relaxation rate vs momentum relaxation rate [8,28]. This employs temperature as the implicit variable, using the data of Figs. 6(a) and 6(b) to plot τ_s^{-1} versus $\tau_{e,ph}^{-1}$, where $\tau_{e, \text{ph}}^{-1}$ is the momentum relaxation time specifically due to phonon scattering [8,28]. This is zero at T=0, then rises monotonically with increasing T as τ_e drops [see Fig. 6(a)]. As expected, the black points in Fig. 6(c), which derive from $\tau_s(T)$ data from $\Delta R_{\rm NL}(d)$ [as for the black points in Fig. 6(b)] are well described by a straight-line fit (solid black line). Based on the E-Y relation [Eq. (1)], this straight line yields $1/\beta_{\rm ph}$ from the slope, and $1/\beta_{\rm def}$ from the intercept, where $\beta_{\rm ph}$ and $\beta_{\rm def}$ are the E-Y constants for electron-phonon and electron-defect scattering, respectively [8,28]. Similarly, the blue points in Fig 6(c) are from the Hanle data in Fig. 6(b), which also generate a straight-line fit, albeit with slightly different β_i . Explicitly, the $\Delta R_{\rm NL}(d)$ data in Fig. 6(c) (black) give $\beta_{\rm ph}=1600\pm160$ and $\beta_{\rm def}=1200\pm40$, while the Hanle data in Fig. 6(c) (blue) give $\beta_{\rm ph} = 3600 \pm 2700$ and $\beta_{\rm def} =$ 900 ± 30 . Discounting the Hanle $\beta_{\rm ph}$ value due to the unacceptably large error generated by the small T range [Figs. 6(b) and 6(c)], we are left with $\beta_{\rm ph} = 1600 \pm 160$ and an average $\beta_{\rm def} = 1050 \pm 50$. (Note that the thickness here is 300 nm, meaning that surface/interface effects can be ignored [28] and these values reflect the bulk). As discussed in the Introduction, in the absence of light-N alloy data to compare to, these values can be compared to $\beta_{\rm ph} = 26\,000$ and $\beta_{\rm def} = 4200$ in Al [27], and $\beta_{ph} = 740$ and $\dot{\beta}_{def} = 240$ (neglecting magnetic impurities, which are apparently not relevant in Al₂Cu) in Cu [8,22,29]. While the Al values are not bettered, encouragingly, these first β values in θ -Al₂Cu are substantially better than in Cu, by a factor of ~ 2.2 for phonon scattering and ~ 4.4 for defect scattering. These are also realized in the absence of Kondo spin relaxation, which is a pervasive issue in Cu-based NLSVs [8,22,23,29,55]. Particularly given the finite compositional window over which θ -Al₂Cu forms (See Fig. 1), additional future effort with defect control could also improve resistivity values, thus obtaining longer λ_N with these β_i .

C. DFT calculations

Insight into the origin of the β_i values determined above was derived from DFT calculations. Figure 7(a) shows the DFT-calculated electronic band structure of θ -Al₂Cu, where the zero of energy is E_F (which is 10.7 eV from the bottom of the conduction band, as noted above), and the results are shown both including and neglecting SOC. As expected, spin-orbit effects are relatively weak (the curves essentially overlap), the system is clearly metallic, and the bands around $E_{\rm F}$ are highly dispersive. These bands carry substantial weight from both Al and Cu, as expected in an intermetallic compound, and have Al-p, Cu-d, and Cu-p orbital character. Based on the discussion of spin relaxation hot spots in Sec. I, of highest interest in terms of spin transport are accidental degeneracies and intersections of the Fermi surface with Brillouin zone boundaries [30–33]. With respect to the former, band crossings are highlighted in Fig. 7(a) with orange circles. While the majority of these arise far from $E_{\rm F}$, and are irrelevant for transport, one crossing occurs close to the Fermi level, as highlighted by the red circle. Figure 7(b) shows a band structure close-up in the vicinity of this point, revealing a crossing within ~ 10 meV of $E_{\rm F}$ without SOC, which becomes gapped by ~ 30 meV when SOC is included. While such small energies are subject to significant errors in DFT, and stoichiometry deviations could shift the exact $E_{\rm F}$, this nevertheless indicates an SOC-lifted degeneracy close to $E_{\rm F}$, highlighted by Fabian and Das Sarma as the most damaging form of spin relaxation hot spot [30–33].

Figure 8(a) then focuses on the next most deleterious form of hot spot [30–33], showing the calculated Fermi surface and first Brillouin zone of θ -Al₂Cu (using different colors and panels for different pockets), and thus the points of intersection of the Fermi surface and Brillouin zone. Such intersections arise on all faces of the Brillouin zone; there are four between the P and X points, which are on the corner and center of the hexagonal faces, and two between the P and N points, which are on the corner and center of one of the quadrilateral faces. Near the P point, the two smallest Fermi pockets cross the Brillouin zone boundary at wavevectors very close to each other, possibly further enhancing spin relaxation. While full quantification would require an almost prohibitively demanding calculation of the influence of these different types of hot spots on the total (Fermi-surface-averaged) β , these DFT results thus provide clear indications of the potential for spin relaxation hot spots in θ -Al₂Cu, qualitatively consistent with the experimental finding that the β_i do not exceed those of Al, for example. For completeness, these DFT calculations of Al₂Cu were repeated with relaxed internal atomic coordinates, and also with relaxed lattice parameters. The lattice parameter relaxations were 0.2–0.5% and were found to result in only very small band structure changes (see Fig. S5 [57]). In particular, the hot spot close to $E_{\rm F}$ persists.

Given the indications of η' -AlCu formation in Figs. 2 and S4 [56] (which was confirmed by XRD), similar DFT

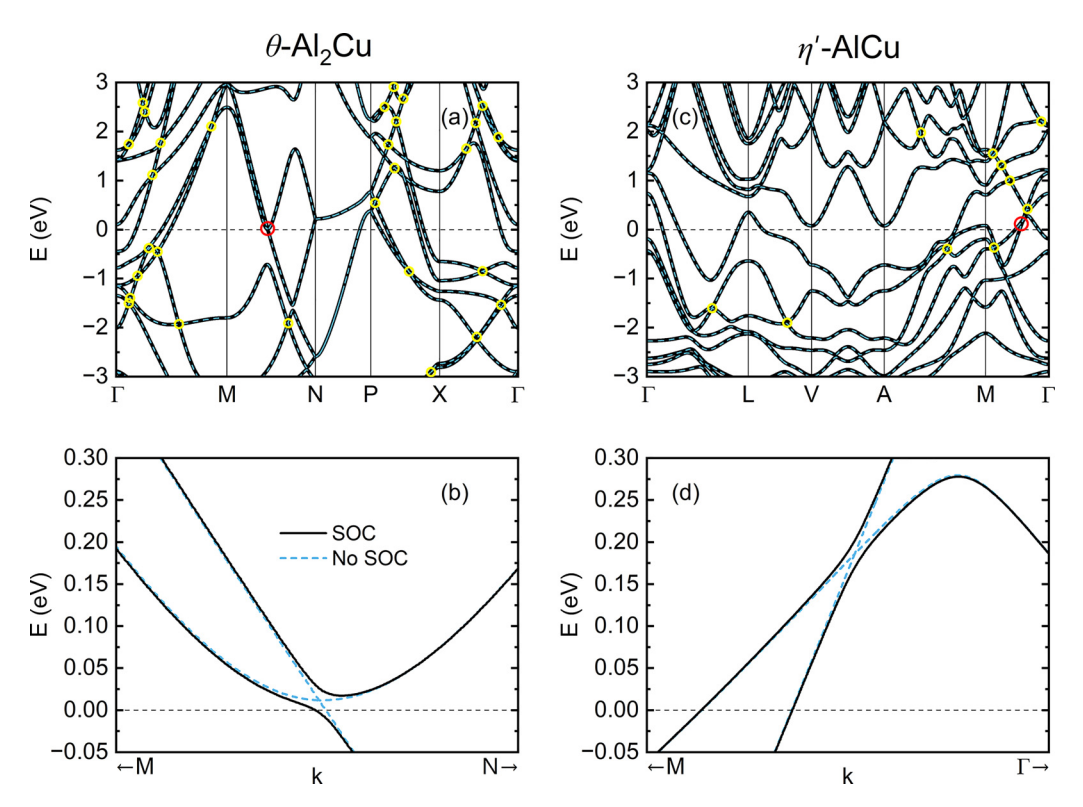


FIG. 7. (a), (c) Electronic band structure of θ -Al₂Cu and η' -AlCu from density functional theory calculations with (black solid lines) and without (blue dashed lines) spin-orbit coupling. The zero of energy is the Fermi level, and band crossings (accidental degeneracies) are highlighted with orange circles (the closest to the Fermi level with a red circle). (b), (d) Close-up band structure around the red circled points in panels (a), (c), i.e., the closest degeneracies to the Fermi level. The points M, N, P, X, and L, V, A, M, are defined in Fig. 8.

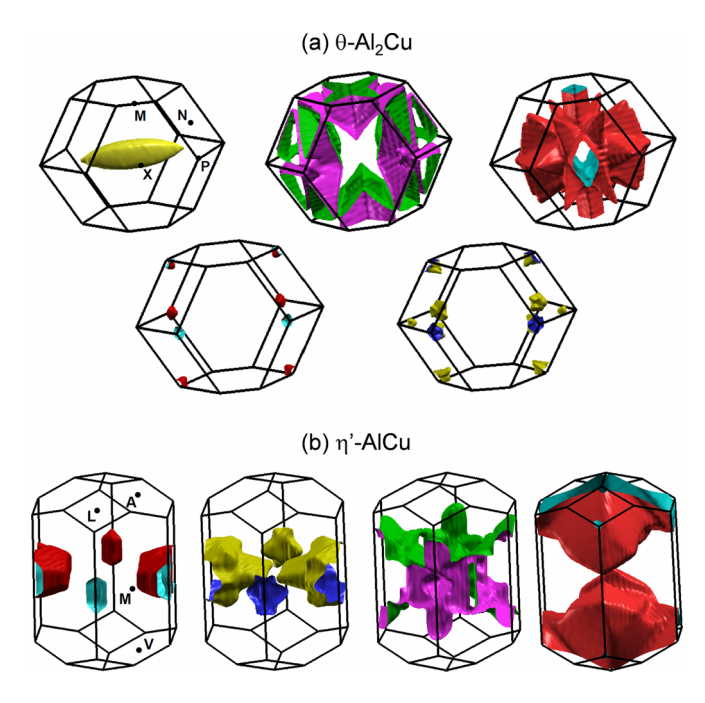


FIG. 8. (a) Fermi surface of θ -Al₂Cu from density functional theory, with the different pockets shown in different panels and colors, for clarity. (b) Fermi surface of η' -AlCu from density functional theory, with the different pockets shown in different panels and colors, for clarity.

calculations were also performed on that phase for comparison. The results are shown in Figs. 7(c), 7(d), and 8(b). Most interestingly, fewer band crossings are visible in Fig. 7(c), the closest to the Fermi level (which is 10.8 eV from the bottom of the conduction band) being 190 meV away, much further than in θ -Al₂Cu, as is clear from comparing the close-ups in Figs. 7(b) and 7(d). Figure 8(b) then shows the calculated η' -AlCu Fermi surface and first Brillouin zone, showing fewer Fermi pockets that cross the Brillouin zone boundary. In particular, there are no pockets that are as small and as close to each other as those at the P point in θ -Al₂Cu. Combining these observations, η' -AlCu appears less likely than θ -Al₂Cu to suffer from spin relaxation hot spots. Again, full quantification of such statements would require highly demanding calculations of the influence of hot spots on the Fermi-surface averaged E-Y parameters in both phases, and so we make only semi-quantitative statements based on the number of hot spot features, their proximity to $E_{\rm F}$, etc. While higher resistivity may be a concern, these findings point to η' -AlCu as a next obvious target of interest for spin transport experimentation in the Al-Cu binary alloy system. More generally, we believe that the work presented in this paper can serve as a foundation for the exploration of spin transport in a variety of other light-metal alloys (in and beyond the Al-Cu system), seeking systems with mitigated spin relaxation hot spots. Theory-driven and data-driven approaches would seem particularly promising for such an endeavour.

IV. SUMMARY

Attempting to expand the exploration of spin transport and relaxation to light-metal alloys, this work first presented on the crystal structure, microstructure, chemical composition, and electronic transport properties of thin films of binary Al-Cu alloys, focusing in particular on the θ phase of Al₂Cu. Single-phase, textured, nanograined polycrystalline thin films of θ -Al₂Cu were demonstrated, and then integrated into θ -Al₂Cu-based nonlocal spin valves. Al₂Cu films with resistivity down to \sim 5 $\mu\Omega$ cm were found to support spin diffusion lengths > 100 nm at low temperatures, with no indication of Kondo effects. Elliott-Yafet constants for spin relaxation by phonon and defect scattering were thus determined, revealing, encouragingly, values that exceed those in Cu by factors of more than 2 and 4, respectively. Complementary electronic structure calculations were then used to semi-quantitatively interpret these results and motivate further exploration of spin transport in the Al-Cu system. These findings represent a promising start to the exploration of nonlocal spin transport in light nonmagnetic alloys, pointing to the potential of both atomically ordered and atomically disordered light alloys for the engineering of large Elliott-Yafet constants and thus longrange spin transport, of high interest both fundamentally and technologically.

All data presented in this paper are available at DRUM (Data Repository for the University of Minnesota) at [66].

ACKNOWLEDGMENTS

This work was primarily supported by the National Science Foundation through Grant No. DMR-2103711. Additional support (for B.K.) from Seagate Technology Inc. and the Advanced Storage Research Committee is acknowledged. Parts of this work were conducted in the Minnesota Nano Center, which is supported by NSF through the National Nanotechnology Coordinated Infrastructure under Grant No. ECCS2025124, and in the UMN Characterization Facility, which is partially supported by NSF through the MRSEC program under Grant No. DMR-2011401. DFT calculations (P.D. and T.B.) were supported by the Department of Energy through the UMN Center for Quantum Materials under Grant No. DE-SC0016371. We acknowledge P. Crowell and L. O'Brien for useful comments and discussions.

- [1] E. Y. Tsymbal and I. Žutić, *Handbook of Spin Transport and Magnetism* (CRC Press, New York, NY, 2016).
- [2] S. Maekawa, S. O. Valenzuela, E. Saitoh, and T. Kimura, *Spin Current* (Oxford University Press, Oxford, UK, 2017).
- [3] F. Hellman, A. Hoffmann, Y. Tserkovnyak, G. S. D. Beach, E. E. Fullerton, C. Leighton, A. H. MacDonald, D. C. Ralph, D. A. Arena, H. A. Dürr, P. Fischer, J. Grollier, J. P. Heremans, T. Jungwirth, A. V. Kimel, B. Koopmans, I. N. Krivorotov, S. J. May, A. K. Petford-Long, J. M. Rondinelli, N. Samarth, I. K. Schuller, A. N. Slavin, M. D. Stiles, O. Tchernyshyov, A. Thiaville, and B. L. Zink, Interface induced phenomena in magnetism, Rev. Mod. Phys. 89, 025006 (2017).
- [4] A. Hirohata, K. Yamada, Y. Nakatani, I.-L. Prejbeanu, B. Diény, P. Pirro, and B. Hillebrands, Review on spintronics: Principles and device applications, J. Magn. Magn. Mater. 509, 166711 (2020).
- [5] Recently also generalized to high-Z metals: A. Kiss, L. Szolnoki, and F. Simon, The Elliott-Yafet theory of spin relaxation generalized for large spin-orbit coupling, Sci. Rep. 6, 22706 (2016).
- [6] R. J. Elliott, Theory of the effect of spin-orbit coupling on magnetic resonance in some semiconductors, Phys. Rev. 96, 266 (1954).
- [7] Y. Yafet, *g* factors and spin-lattice relaxation of conduction electrons, Solid State Phys. **14**, 1 (1963).
- [8] J. D. Watts, L. O'Brien, J. S. Jeong, K. A. Mkhoyan, P. A. Crowell, and C. Leighton, Magnetic impurities as the origin of the variability in spin relaxation rates in Cu-based spin transport devices, Phys. Rev. Mater. 3, 124409 (2019).
- [9] F. Beuneu and P. Monod, The Elliott relation in pure metals, Phys. Rev. B 18, 2422 (1978).
- [10] P. Monod and F. Beuneu, Conduction-electron spin flip by phonons in metas: Analysis of experimental data, Phys. Rev. B 19, 911 (1979).

- [11] J. Bass and W. P. Pratt, Spin-diffusion lengths in metals and alloys, and spin-flipping at metal/metal interfaces: An experimentalist's critical review, J. Phys.: Condens. Matter Phys. 19, 183201 (2007).
- [12] M. Johnson and R. H. Silsbee, Interfacial charge-spin coupling: Injection and detection of spin magnetization in metals, Phys. Rev. Lett. 55, 1790 (1985).
- [13] F. J. Jedema, A. T. Filip, and B. J. van Wees, Electrical spin injection and accumulation at room temperature in an all-metal mesoscopic spin valve, Nature (London) 410, 345 (2001).
- [14] F. J. Jedema, M. S. Nijboer, A. T. Filip, and B. J. van Wees, Spin injection and spin accumulation in allmetal mesoscopic spin valves, Phys. Rev. B 67, 085319 (2003).
- [15] S. O. Valenzuela and M. Tinkham, Spin-polarized tunneling in room-temperature mesoscopic spin valves, Appl. Phys. Lett. 85, 5914 (2004).
- [16] Y. Ji, A. Hoffmann, J. S. Jiang, and S. D. Bader, Spin injection, diffusion, and detection in lateral spin-valves, Appl. Phys. Lett. 85, 6218 (2004).
- [17] T. Kimura, T. Sato, and Y. Otani, Temperature evolution of spin relaxation in a NiFe/Cu lateral spin valve, Phys. Rev. Lett. 100, 066602 (2008).
- [18] M. Erekhinsky, A. Sharoni, F. Casanova, and I. K. Schuller, Surface enhanced spin-flip scattering in lateral spin valves, Appl. Phys. Lett. **96**, 022513 (2010).
- [19] Y. Fukuma, L. Wang, H. Idzuchi, and Y. Otani, Enhanced spin accumulation by inserting low-resistance MgO interface in metallic lateral spin valves, Appl. Phys. Lett. 97, 012507 (2010).
- [20] G. Mihajlović, J. E. Pearson, S. D. Bader, and A. Hoffmann, Surface spin flip probability of mesoscopic Ag wires, Phys. Rev. Lett. 104, 237202 (2010).

- [21] E. Villamor, M. Isasa, L. E. Hueso, and F. Casanova, Contribution of defects to the spin relaxation in copper nanowires, Phys. Rev. B **87**, 094417 (2013).
- [22] L. O'Brien, M. Erickson, D. Spivak, H. Ambaye, R. J. Goyette, V. Lauter, P. A. Crowell, and C. Leighton, Kondo physics in non-local metallic spin transport devices, Nat. Commun. 5, 3927 (2014).
- [23] J. T. Batley, M. C. Rosamond, M. Ali, E. H. Linfield, G. Burnell, and B. J. Hickey, Spin relaxation through Kondo scattering in Cu/Py lateral spin valves, Phys. Rev. B 92, 220420(R) (2015).
- [24] H. Idzuchi, Y. Fukuma, and Y. Otani, Spin transport in non-magnetic nano-structures induced by nonlocal spin injection, Physica E **68**, 239 (2015).
- [25] G. Zahnd, L. Vila, V. T. Pham, M. Cosset-Cheneau, W. Lim, A. Brenac, P. Laczkowski, A. Marty, and J. P. Attané, Spin diffusion length and polarization of ferromagnetic metals measured by the spin-absorption technique in lateral spin valves, Phys. Rev. B 98, 174414 (2018).
- [26] Y. Cai, C. Qin, F. Kandaz, X. Shen, C. Zhou, M. Jia, Y. Luo, Y. Wu, and Y. Ji, Quantifying spin relaxation in mesoscopic Cu channels via a multitude of nonlocal spin valves, Phys. Rev. B 100, 144419 (2019).
- [27] S. Rakheja, S.-C. Chang, and A. Naeemi, Impact of dimensional scaling and size effects in spin transport in copper and aluminum interconnects, IEEE Trans. Electron Devices 60, 3913 (2013).
- [28] J. D. Watts, J. T. Batley, N. A. Rabideau, J. P. Hoch, L. O'Brien, P. A. Crowell, and C. Leighton, Finite-size effect in phononinduced Elliott-Yafet spin relaxation in Al, Phys. Rev. Lett. 128, 207201 (2022).
- [29] K.-W. Kim, L. O'Brien, P. A. Crowell, C. Leighton, and M. D. Stiles, Theory of Kondo suppression of spin polarization in nonlocal spin valves, Phys. Rev. B 95, 104404 (2017).
- [30] J. Fabian and S. Das Sarma, Spin relaxation of conduction electrons in polyvalent metals: Theory and a realistic calculation, Phys. Rev. Lett. **81**, 5624 (1998).
- [31] J. Fabian and S. Das Sarma, Phonon-induced spin relaxation of conduction electrons in aluminum, Phys. Rev. Lett. 83, 1211 (1999)
- [32] J. Fabian and S. Das Sarma, Spin relaxation of conduction electrons, J. Vac. Sci. Technol. B 17, 1708 (1999).
- [33] J. Fabian and S. Das Sarma, Band-structure effects in the spin relaxation of conduction electrons, J. Appl. Phys. **85**, 5075 (1999).
- [34] M. Takagishi, K. Yamada, H. Iwasaki, H. N. Fuke, and S. Hashimoto, Magnetoresistance ratio and resistance area design of CPP-MR film for 2–5 Tb/in² read sensors, IEEE Trans. Magn. **46**, 2086 (2010).
- [35] Y. K. Takahashi, S. Kasai, S. Hirayama, S. Mitani, and K. Hono, All-metallic lateral spin valves using $Co_2Fe(Ge_{0.5}Ga_{0.5})$ Heusler alloy with a large spin signal, Appl. Phys. Lett. **100**, 052405 (2012).
- [36] M. Yamada, D. Sato, N. Yoshida, M. Sato, K. Meguro, and S. Ogawa, Scalability of spin accumulation sensor, IEEE Trans. Magn. 49, 713 (2013).
- [37] T. Nakatani, Z. Gao, and K. Hono, Read sensor technology for ultrahigh density magnetic recording, MRS Bull. 43, 106 (2018).

- [38] G. Albuquerque, S. Hernandez, M. T. Kief, D. Mauri, and L. Wang, HDD reader technology roadmap to an areal density of 4 Tbpsi and beyond, IEEE Trans. Magn. 58, 1 (2022).
- [39] S. Takahashi and S. Maekawa, Spin injection and detection in magnetic nanostructures, Phys. Rev. B 67, 052409 (2003).
- [40] S.-C. Chang, S. Manipatruni, D. E. Nikonov, I. A. Young, and A. Naeemi, Design and analysis of Si interconnects for all-spin logic, IEEE Trans. Mag. **50**, 3400513 (2014).
- [41] O. Zobac, A. Kroupa, A. Zemanova, and K. W. Richter, Experimental description of the Al-Cu binary phase diagram, Metall. Mater. Trans. A 50, 3805 (2019).
- [42] N. Ponweiser, C. L. Lengauer, and K. W. Richter, Reinvestigation of phase equilibria in the system Al-Cu and structural analysis of the high-temperature phase η_1 -Al_{1- δ}Cu, Intermetallics **19**, 1737 (2011).
- [43] R. E. Smallman and A. H. W. Ngan, *Modern Physical Metallurgy* (Butterworth-Heinemann, Oxford, UK, 2013).
- [44] C. Macchioni, J. A. Rayne, S. Sen, and C. L. Bauer, Low temperature resistivity of thin film and bulk samples of CuAl₂ and Cu₉Al₄, Thin. Solid. Films **81**, 71 (1981).
- [45] L. Chen, D. Ando, Y. Sutou, and J. Koike, CuAl₂ thin films as a low-resistivity interconnect material for advanced semiconductor devices, J. Vac. Sci. Technol. B **37**, 031215 (2019).
- [46] M. Zhang and D. Gall, Resistivity scaling in epitaxial CuAl₂(001) layers, IEEE Trans. Electron Devices 69, 5110 (2022).
- [47] J.-P. Soulie, Z. Tokei, J. Swerts, and C. Adelmann, Aluminide intermetallics for advanced interconnect metallization: Thin film studies, in *Proceedings of the IEEE International Inter- connect Technology Conference (IITC'21)* (IEEE, Kyoto, Japan, 2021).
- [48] C. Macchioni, J. A. Rayne, and C. L. Bauer, Low-temperature resistivity of bulk copper-aluminum alloys, Phys. Rev. B 25, 3865 (1982).
- [49] J. Koike, T. Kuge, L. Chen, and M. Yahagi, Intermetallic compounds for interconnect metal beyond 3 nm node, in *Proceedings of the IEEE International Interconnect Technology Conference (IITC'21)* (IEEE, Kyoto, Japan, 2021).
- [50] L. Chen, S. Kumar, M. Yahagi, D. Ando, Y. Sutou, D. Gall, R. Sundararaman, and J. Koike, Interdiffusion reliability and resistivity scaling of intermetallic compounds as advanced interconnect materials, J. Appl. Phys. 129, 035301 (2021).
- [51] T. Kuge, M. Yahagi, and J. Koike, CuAl intermetallic compound for Cu alternative, J. Alloys Compd. 918, 165615 (2022).
- [52] T. Kuge, M. Yahagi, and J. Koike, Effects of composition deviation of CuAl₂ on BTS and TDDB reliability, in *Proceedings of the IEEE International Interconnect Technology Conference* (IITC'21) (IEEE, Kyoto, Japan, 2021).
- [53] T. Kuge, M. Yahagi, and J. Koike, A comprehensive evaluation of time-dependent dielectric breakdown of CuAl₂ on SiO₂ for advanced interconnect applications, IEEE Trans. Device Mater. Reliab. 24, 14 (2024).
- [54] B. Pittenger, N. Erina, and S. Chanmin, Quantitative Mechanical Property Mapping at the Nanoscale with PeakForce QNM, Application Note (Veeco Instruments Inc., Plainview, NY, 2010).
- [55] J. D. Watts, J. S. Jeong, L. O'Brien, K. A. Mkhoyan, P. A. Crowell, and C. Leighton, Room temperature spin Kondo effect and intermixing in Co/Cu nonlocal spin valves, Appl. Phys. Lett. 110, 222407 (2017).

- [56] B. Kaiser, J. Ramberger, J. D. Watts, J. Dewey, Y. Zhang, and C. Leighton, High spin polarization and spin signal enhancement in non-local spin valves with Co–Fe alloy injectors and detectors, APL Mater. 11, 051108 (2023).
- [57] See Supplemental Material at http://link.aps.org/supplemental/ 10.1103/PhysRevMaterials.8.114416 for additional device fabrication details, further composition-dependent SEM images, example two-dimensional X-ray diffraction data, additional AFM images, and supporting DFT calculations.
- [58] P. Blaha, K. Schwarz, F. Tran, R. Laskowski, G. K. H. Madsen, and L. D. Marks, WIEN2k: An APW+lo program for calculating the properties of solids, J. Chem. Phys. 152, 074101 (2020).
- [59] J. P. Perdew, K. Burke, and M. Ernzerhof, Generalized gradient approximation made simple, Phys. Rev. Lett. 77, 3865 (1996).
- [60] M. El-Boragy, R. Szepan, and K. Schubert, Crystal structure of Cu₃Al₂ and CuAl, J. Less-Common Metals 29, 133 (1972).

- [61] A. Meetsma, J. L. De Boer, and S. Van Smaalen, Refinement of the crystal structure of Al₂Cu, J. Solid State Chem. 83, 370 (1989).
- [62] S. O. Kasap, Principles of Electronic Materials and Devices (McGraw Hill, New York, NY, 2018).
- [63] T. Valet and A. Fert, Theory of the perpendicular magnetoresistance in magnetic multilayers, Phys. Rev. B 48, 7099 (1993).
- [64] L. O'Brien, D. Spivak, N. Krueger, T. A. Peterson, M. J. Erickson, B. Bolon, C. C. Geppert, C. Leighton, and P. A. Crowell, Observation and modelling of ferromagnetic contact-induced spin relaxation in Hanle spin precession measurements, Phys. Rev. B 94, 094431 (2016).
- [65] F. Izumi and K. Momma, VESTA3 for three-dimensional visualization of crystals, volumetric and morphology data, Appl. Crystallogr. 44, 1272 (2011).
- [66] https://hdl.handle.net/11299/266673.